Quantifying local stiffness and forces in soft biological tissues using droplet optical microcavities

Gregor Pirnat[a,b], Matevž Marinčič[a,b], Miha Ravnik[b,a], and Matjaž Humar[a,b,c]

[a] *Condensed Matter Department, J. Stefan Institute, Jamova 39, SI-1000 Ljubljana, Slovenia*

[b] *Faculty of Mathematics and Physics, University of Ljubljana, Jadranska 19, SI-1000, Ljubljana, Slovenia*

[c] *CENN Nanocenter, Jamova 39, SI-1000 Ljubljana, Slovenia*

**E-mail: matjaz.humar@ijs.si*

Abstract

Mechanical properties of biological tissues fundamentally underlie various biological processes and non-contact, local, and microscopic methods can provide fundamental insights. Here, we present a novel approach for quantifying the local mechanical properties of biological materials at the microscale, based on measuring the spectral shifts of the optical resonances in droplet microcavities. Specifically, the developed method allows for measurements of deformations in dye-doped oil droplets embedded in soft materials or biological tissues with an error of only 1 nm, which in turn enables measurements of anisotropic stress inside tissues as small as a few pN/μm^2. Furthermore, by applying an external strain, Young's modulus can be measured in the range from 1 Pa to 35 kPa, which covers most human soft tissues. Using multiple droplet microcavities, our approach could enable mapping of stiffness and forces in inhomogeneous soft tissues and could also be applied to in vivo and single-cell experiments. The developed method can potentially lead to new insights into the mechanics of biological tissues.

Significance Statement: Due to the importance of mechanical processes in biological organisms there have been a large variety of methods developed to study these processes. However, most of these methods are limited to measuring only one parameter at a time and frequently do not enable measurement inside tissues. By using optical resonances in droplets we are able to measure the deformations of these liquid inclusions to a nanometer accuracy, almost 100 times better than today's state-of-the-art confocal microscopy. This enables quantitative long-term spatial mapping of both the absolute stiffness and forces. Furthermore, the developed approach has the potential to serve as a powerful multimodal probe, enabling simultaneous mechanical mapping, refractive index measurement, and acting as micro barcodes.

Keywords: microdroplets, whispering gallery modes, stiffness, biological tissues, liquid inclusions

Introduction

Microscopic mechanical properties and forces are central in diverse materials and material applications, ranging from soft matter [1], microrheology of complex fluids [2] to biological tissues [3], tissue regeneration and bio-engineering [4]. Distinctly in biology, the forces acting in living organisms play crucial roles in various developmental, homeostatic, and pathological processes [3, 5], such as cell differentiation and tumor growth. The role of mechanics is often insufficiently understood, partially because of the limitations of the current measurement techniques. Multiple techniques are used to measure the viscoelastic properties of cells and tissues and forces acting within them [6, 7], including atomic force microscopy [8], traction force microscopy [9–11], arrays of micropillars [12, 13], optical tweezers [14] and Brillouin microscopy [15]. Frequently, in these force measurement techniques, the cells are placed in contact with an artificial material and are spatially isolated to individual cells or cell monolayers. However, cells require a complex biophysical and biochemical environment to behave in a truly physiologically realistic manner, which is only achievable in a 3D extracellular matrix or in vivo. Therefore, a truly non-contact force measurement is needed of cells surrounded only by the biological environment.

Recently, new methods have been developed to measure cell-generated mechanical forces within living tissues using cell-sized oil microdroplets injected between the cells [16, 17], cell-generated stresses in a microchannel using emulsion droplets [18] and by spheroid-generated stresses using deformable hydrogel microdroplets [19]. The droplet deformation within a deformed material is governed by the ratio between the interfacial tension and Young's modulus. This ratio, also known as the elastocapillary length, is an important parameter, especially in soft materials and biological tissues. It affects the surface deformation of soft solids [20, 21], fabrication of solid-liquid composites via 3D printing [22], development of smart materials [23–25], mechanical interaction between implants and surrounding tissues [26], and governs the morphology of single cells [27].

Spherical microresonators that support photonic whispering gallery modes (WGMs) can be used as very precise sensors and are sensitive to changes in refractive index and shape of the microresonator [28–31]. Specifically, droplet microresonators and microresonators made of soft materials, which easily adapt their shape to external forces while maintaining smooth surface, have been used as tunable light sources [32,33], lasers [34–36], force sensors [37], probes for measuring surface tension [38], as well for single particle detection [39, 40]. However, there are only a few applications of WGM to study tissue mechanics. For example, anisotropic stress was measured inside cells [41] and the biological strain of bones was determined [42].

In this paper, we demonstrate a WGM-based method for measuring local stiffness and forces in soft and biological materials via droplet deformations. The introduction of the droplet into tissues is minimally invasive and after the injection the measurements are non-contact. Our approach enables the measurement of ~ 2 orders of magnitude smaller droplet deformations compared to state-of-the-art confocal microscopy [16]. We can measure deformations as small as a few nanometers, whereas the measurement error in droplet curvature measurement by other microscopy is in the order of several 100 nm. Measurement of both anisotropic stress and Young's modulus of the material was demonstrated, which is also quite unique compared to other techniques, where usually only one parameter is measured at a time. We also show that the method is viable in a wide range of stiffnesses.

Results and discussion

The developed experimental method for measuring the mechanical properties of tissues consists of injecting an oil droplet into a tissue, exciting the WGMs within the droplet, collecting the spectra, and analyzing the spectral shifts (Figure 1). One or multiple dye-doped oil droplets with sizes of the order of 10 µm are controllably injected into the tissue to a well-controlled position (Figure 1a) or dispersed in a soft material. The maximum pressure needed for injection is used to measure the interfacial tension. Whispering gallery modes are excited via external illumination and spectra are collected at different positions in the droplet (Figure 1b). Due to forces acting within the tissue, the droplet gets deformed from the perfectly spherical shape preferred by the surface tension (Figure 1c). By measuring spectral shifts of WGMs circulating in different planes in the droplet (Figure 1d), the deformation amplitude and direction can be quantified. Finally, combining the measured deformations with numerical simulations enables us to relate the droplet size, droplet deformation, Young's modulus, strain, and interfacial tension. In this work, to validate the method, the measurements are first performed in soft hydrogels with known mechanical properties and by applying a controlled external strain. The used gelatine hydrogel has Young's modulus of 1.6 kPa which is similar to the stiffness of soft biological materials such as brain 1-10 kPa [43–45] and fat tissue 1-4.5 kPa [46].

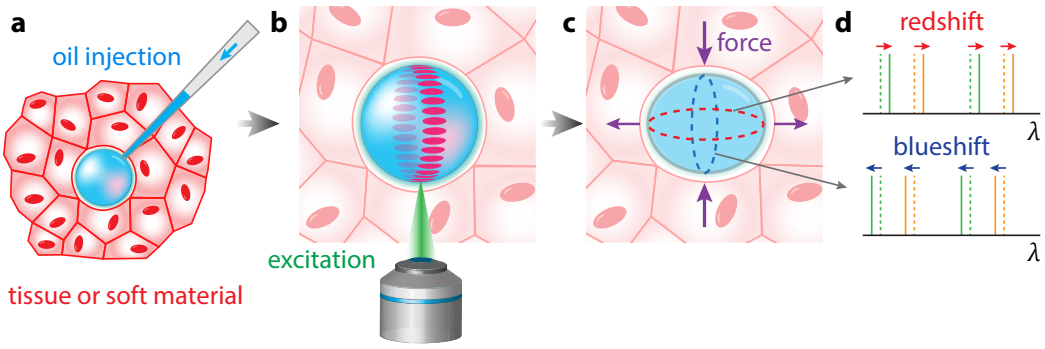

Figure 1. Schematic illustration of the experimental workflow. **(a)** A droplet is injected into the investigated material via a microcapillary. **(b)** Droplet acts as an optical microcavity when its optical resonances are excited by an external light source. **(c)** The droplet deforms due to external forces, whereas the interfacial tension resists droplet deformation. **(d)** The measured WGM wavelengths are dependent on the optical path length: any droplet deformation results in a redshift or a blueshift depending on whether the circumference in that plane increases or decreases, respectively.

Droplet deformation in hydrogel

The experimental setup consisted of a rectangular glass container filled with a dispersion of fluorescent dye-doped oil microdroplets ($n = 1.62$) in a gelatin-based hydrogel (Figure 2a). The hydrogel containing the droplets was deformed by a movable wall, connected to a linear motorized stage. The sample was compressed or stretched in the x-direction. In the y-direction the hydrogel was restricted by the walls of the container. In z-direction the bottom was closed by the glass slide, while the top surface of the hydrogel was free to move up and down. The droplet dispersion was prepared in two stages, as described in the methods section so that the polydispersed microdroplets were situated in a single horizontal plane (Figure 2b). By positioning the droplets in a single plane

all droplets are in focus, which enables all their positions and shapes to be tracked simultaneously. Furthermore, this reduces the overall number of oil droplets in the hydrogel, thus minimizing their effect on Young's modulus of the composite material [47]. Alternatively, the droplets can also be injected via microcapillary to a specific position in a three-dimensional volume.

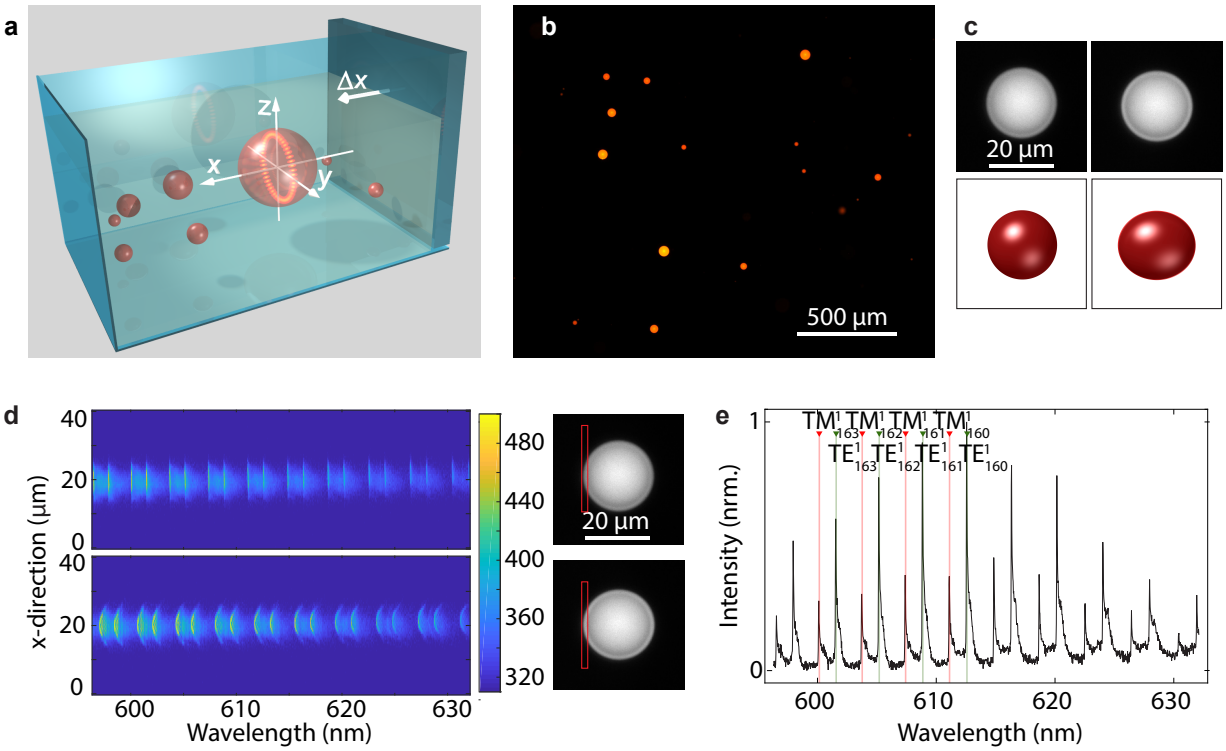

Figure 2. Droplet deformation in a hydrogel. **(a)** Schematic illustration of the experimental setup. A wall moves in x-direction deforming the hydrogel, which contains oil droplets. **(b)** Fluorescence image of microdroplets which are randomly distributed within a single plane in the hydrogel. **(c)** Droplet before induced deformation (left) and deformed droplet (right) at 0 and 2.8% deformation of the hydrogel, with a schematic of the droplet's shape with exaggerated deformation (20× magnified) to assist visualization of the measurement concept. **(d)** Spatially resolved spectra along the spectrometer slit (red rectangle) positioned across a single droplet without induced deformation (top) and a deformed droplet (bottom). **(e)** Typical spectrum at a single point on the droplet's rim without induced deformation.

The wall was moved in steps of typically 50 µm. At each step two measurements were taken: a fluorescence image in a wider field of view and a hyperspectral fluorescence image of the droplet of interest. The fluorescence image containing multiple droplets in the surroundings of the droplet of interest was used to determine the local strain of the hydrogel (Supplementary Figure 1). This was achieved by tracking the relative positions of the droplets with a 0.5 µm error. Instead of using multiple droplets, additional small fluorescent particles could be used to measure local strain with a higher spatial resolution, as it is usually done in traction force microscopy [48]. For the hydrogel far from any wall of the container, the y-component of the measured strain was negligible, whereas the x-component was in agreement with the displacement of the movable wall. At the largest applied strain of 4% the droplet deformations were too small to be resolved by imaging alone (Figure 2c); therefore, WGM measurements were needed and applied for further investigation.

Whispering gallery mode measurements

The hyperspectral scans were first made for samples without induced deformation by the movable wall (Figure 2d-top). In this case, the maximum WGMs shift along the droplet's rim is only ∼0.05 nm (Supplementary Figure 2). In this state, already higher order modes can also be observed all around the droplet's rim as asymmetrically broadened peaks (Figure 2e), which indicates that the droplet is somewhat compressed in the $z-$direction. However, since this semi-axis r_z is common for all modes that radiate in the z-direction, r_z is less relevant and only contributes a small error to the final result (Supplementary Information). The droplet size is then determined by fitting the TE and TM modes [49] to the first-order azimuthal WGMs and verified with the camera image of the droplet.

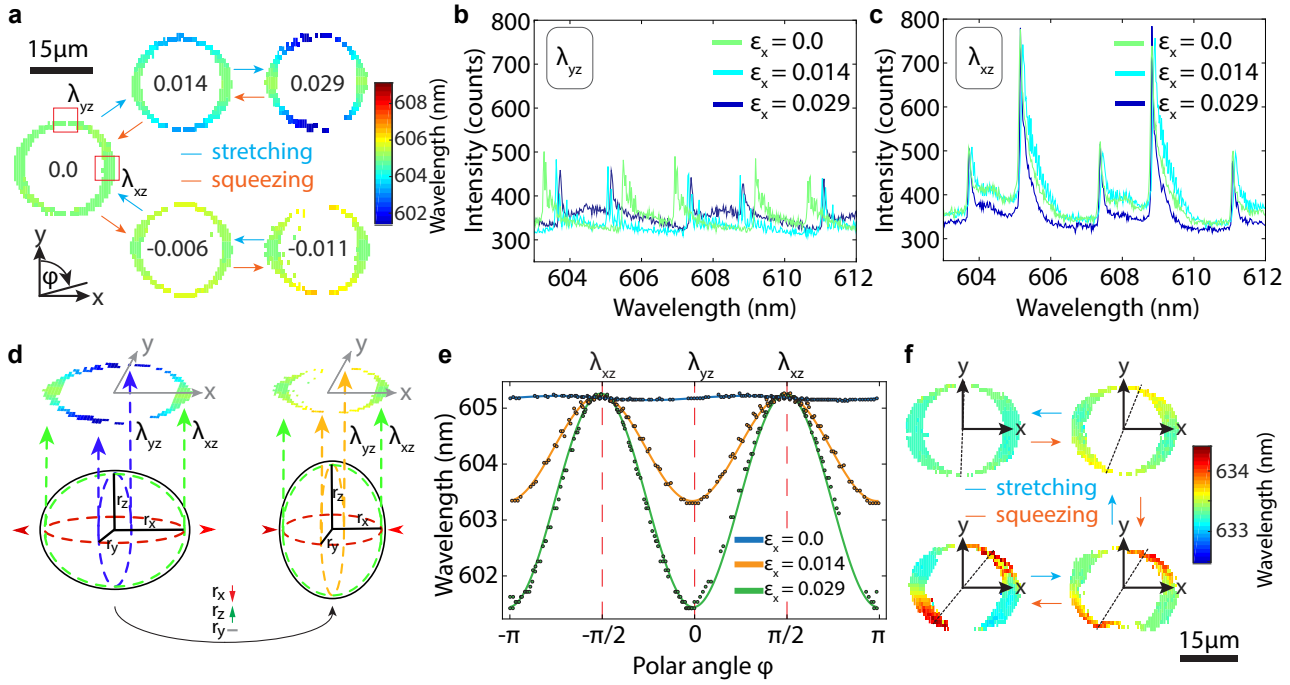

Figure 3. Experimental measurements of droplet deformation via shifts of WGMs. **(a)** Measured wavelength shift of a single WGM peak at different points on the rim of the droplet. The hydrogel surrounding the droplet was stretched up to a strain of $\epsilon = 0.029$ and squeezed up to $\epsilon = -0.011$. The top row represents droplet extension and the bottom row droplet compression. **(b)** Droplet spectra from xz- and **(c)** yz-plane, at different strains. **(d)** Geometry of the droplet deformation is represented by the ellipsoid with semi-axes (r_x, r_y and r_z), planes of the WGMs circulation (green, blue and orange dashed lines) and the WGM wavelengths corresponding to these planes (λ_{yz} and λ_{xz}). Red dashed lines correspond to the droplet circumference as observed through the microscope. The superimposed wavelength shifts at the top belong to the same droplet as figures **a-e**. **(e)** Wavelength shifts from **a** (top row) fitted to an ellipse in polar coordinates at three different strains. **(f)** WGM shifts at different points on the rim of a diagonally deformed droplet.

The hydrogel was deformed which caused a local strain ϵ. This deformation led to different shifts in the WGMs around the droplet's rim (Figure 3a). The shifts are also very distinctly visible in a single-line scan when the spectrometer slit is aligned with the edge of the droplet. The shifts appear as crescent shapes (Figure 2d). When the droplet is stretched the WGMs along the y-direction (λ_{yz}) blueshift (Figure 3b), while conversely when the droplet is compressed the modes redshift. The modes in the x-direction (λ_{xz}) (Figure 3c) do not shift

in either stretching or compressing. This is expected for the geometry in our experiment, where the external strain deforms the hydrogel in the xz plane but not in the y direction. In this geometry, all three axes of the ellipsoid (r_x, r_y, and r_z) can be determined from the spectral shifts on a single hyperspectral image. The relation between the ellipsoid shape and spectral shifts is given in the Supplementary Information. To determine the droplet aspect ratio in the xy-plane r_x/r_y only the measurements of the minimum and maximum wavelength shifts are required. However, because a hyperspectral scan is performed, all spectra along the circumference can be used for a more precise analysis (Figure 3d and e), improving the measurement of both the magnitude and the direction of the deformation. Finally, this also enables us to determine if the deformation is indeed of an ellipsoid shape. Figure 3e shows jointly the three results by plotting the wavelength of a single optical mode as a function of the polar angle $\lambda(\varphi)$ around the droplet rim. The measured data agrees well with the equation of an ellipse, meaning that the droplet is deformed into an ellipsoid shape, at least for small external strains. The simulations also confirm the ellipsoid shape.

The error in measuring the droplet deformation was determined as the fitting error of the amplitude of the ellipsoid curve in Figure 3e. The error determined in this way includes the contributions from the noise, the spectral resolution of the spectrometer, and any deviations from an elliptical shape. The fitting error translates to a distinguishable relative change in the droplet's semi-axis of about 1 nm.

From the shift of the $\lambda(\varphi)$ curve the deformation direction can be determined as well. While in the first example (Figure 3e) the deformation is exactly along the axis, the droplets near the container side wall experience a diagonal deformation (Figure 3f). The deformation angle increases from 2° to 35° when the external strain is increased.

Determination of Young's modulus

The deformation of liquid inclusions in a cubic sample of the elastic material (hydrogel) was simulated to corroborate the experimental results and to relate them to the mechanic properties. The free energy minimization was implemented with finite elements method (FEM). The semi-axes and the droplet aspect ratio are determined by fitting an ellipse to the cross-section of the droplet, confirming the tri-axial ellipsoidal shape as described in the previous section. The details about the simulation are discussed in the Methods section and Supplementary Information.

The experimental data showing the dependence of droplet aspect ratio $\eta = r_x/r_y$ to hydrogel strain ϵ was fitted with a linear function to determine the slope coefficients $k = \Delta\eta/\Delta\epsilon$ which vary for different sized droplets (Figure 4a). The droplet aspect ratio η is calculated from the experimentally measured wavelength shifts, as discussed in the previous section. Due to the experimental error in hydrogel strain measurements (Supplementary Figure 3) the reference state without induced deformation is not precisely determined, which is why the linear fits in experimental data can have nonzero droplet deformation at zero strain. The occasional pre-strain as measured by WGMs of the droplets without deliberately induced deformation was only observed in the $x-$direction and is not problematic since only the slope of the linear fit k is used in our measurement technique, and does not change in the case of strain offset.

The linear dependency is reproduced in the simulation by increasing the strain in the same range as in the experiments (Figure 4b). In the simulations, the interfacial tension γ and the droplet size r are fixed and Young's modulus E is varied. As expected, a stiffer hydrogel will increase the droplet aspect ratio at the same

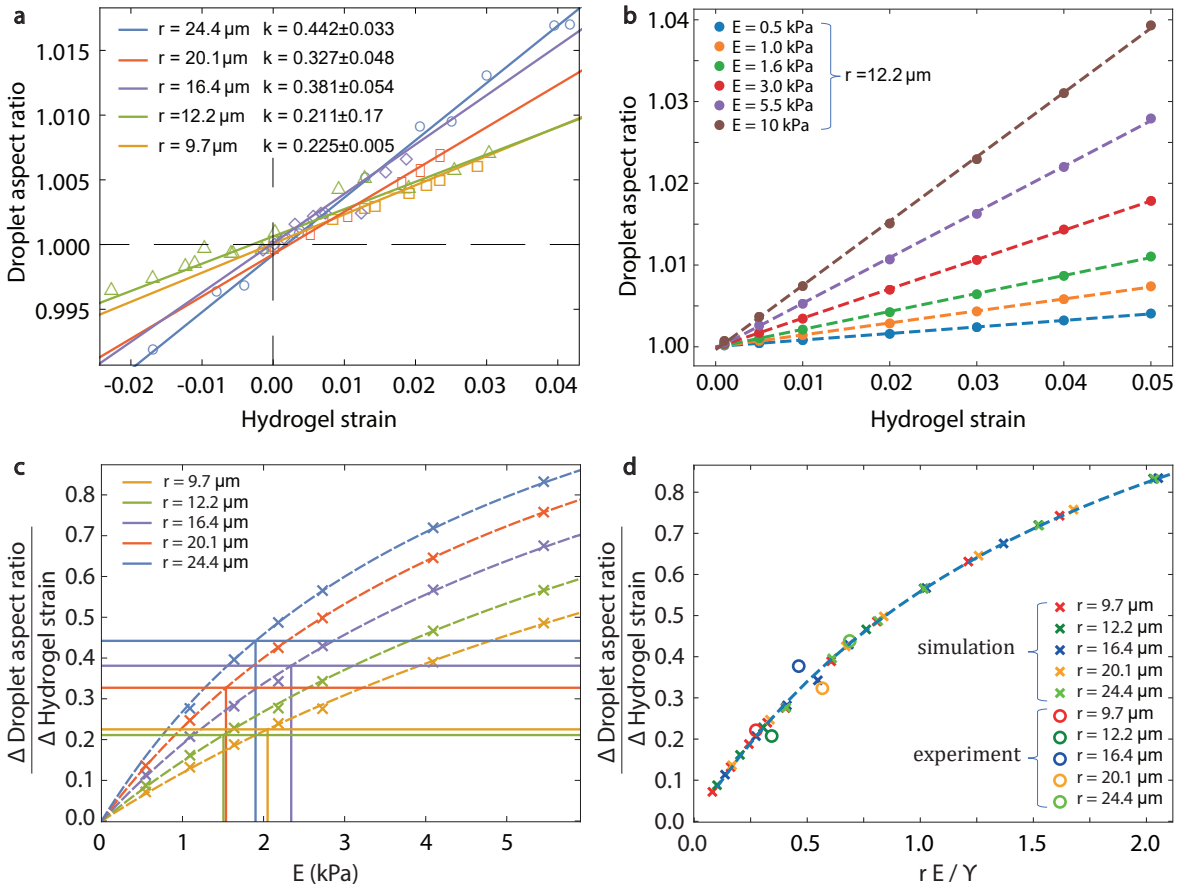

Figure 4. Data analysis and material parameter extraction. **(a)** Experimental measurements of deformation of droplets with different radii r as the external hydrogel strain is increased. **(b)** Droplet aspect ratio $\eta = r_x/r_y$ with respect to the average hydrogel strain ϵ far from the droplet for simulations of one droplet with radius r =12.2 µm and different elastic moduli E. The slope of the linear fit $k = \Delta\eta/\Delta\epsilon$ is calculated for both experimental and simulation results and plotted in **(c,d)**. **(c)** Simulated results for varying elastic moduli E and experimentally measured droplet radii r are represented by crosses and connected with a dashed line. Experimental measurements corresponding to the same droplet sizes are shown as horizontal lines with matching colors. The intersection of the horizontal lines and curved lines for each specific droplet radius indicates the measured Young's modulus E. **(d)** Experimental and simulated data on the same curve, and plotted against the dimensionless quantity rE/γ, which gives the final results $E = 1800\,\mathrm{Pa}$ and $\gamma = 65\,\mathrm{mN/m}$.

hydrogel strain, as the effect of interfacial tension becomes less important.

The simulations were repeated for the same droplet radii, as used in the experiments. The slopes of the linear fits k are used to relate the simulations to the experiments. The slope k increases with Young's modulus E (Figure 4c). Larger droplets deform more at the same material parameters. Each experimental measurement for a different droplet radius is represented by a horizontal line (Figure 4c) and fits a specific Young's modulus. The average across five experimental measurements gives the elastocapillary length $\gamma/E = 35.3\,\mu\mathrm{m}$.

To determine Young's modulus from the elastocapillary length, the interfacial tension has to be known or measured. Because the absorption of surfactant molecules on the oil droplet can significantly change the interfacial tension, it is best to measure it locally. For this reason the maximum bubble pressure tensiometry method [50, 51] was used. A microcapillary is inserted into the material and pressure is gradually increased

until an oil droplet is generated. The interfacial tension is calculated by the Laplace equation $\gamma = p_{\max}/D$, where $p_{\max}$ is the pressure inside the microcapillary needed to create the droplet and D is the microcapillary inner diameter. Because the inner microcapillary diameter of 0.5 µm is much smaller than the elastocapillary length 35 µm, the contribution of elasticity can be neglected. From the maximum pressure of 1350 ± 100 mbar the interfacial tension was measured to be 65 ± 5 mN/m. Notably, this method for locally measuring the interfacial tension between the droplet and the embedding material comes with the advantage of more accurate measurements, as the actual value can vary even inside the tissue. From our measurements, the variation inside the gelatin hydrogel was about 10%, and inside tissues was about 20%.

Taking into account the measured elastocapillary length γ/E the final result for Young's modulus of the hydrogel averaged over 5 droplets is $E = 1800 \pm 300$ Pa. This matches very well with the value measured by the indentation ($E = 1700 \pm 600$ Pa). The error of the measured stiffness both with droplets and with the indentation is mainly due to the variability of the samples, as evident also in other studies [52]. Here, it is worth pointing out that the optical resonances were essential for measuring Young's modulus because the droplet deformation due to external strain has to be measured with an error of less than 10 nm, which is too small for optical imaging.

The results can also be represented together on a single curve (Figure 4d) by plotting the slope k as a function of a dimensionless quantity rE/γ. This quantity is the key scaling parameter and the solutions for different combinations of parameters E, γ, and r fall on the same curve, in line with known literature on liquid inclusions in soft materials [47]. In our experiment, as is the case with μm-sized droplets in many biologically relevant materials, both interfacial energy and elastic strain energy contribution are equally important ($rE/\gamma \sim 1$), which enables the measurement of the material parameters through this method, specifically the elastocapillary length γ/E.

The observed dependence of the droplet aspect ratio on material parameters eventually reaches Eshelby's limit for liquid inclusion without interfacial tension [53], when all liquid inclusions deform at the same rate regardless of their size r, which is seen in Figure 4d as the profile levels off for larger droplets $r \gg \gamma/E$. Actually, this sets the upper limit for measuring elastocapillary length γ/E, when the effect of surface tension becomes negligible and the measurement of Young's modulus is not possible. However, this limit can be used for measuring material strain directly through WGM measurements, as the dependence between droplet aspect ratio and material strain is linear. Material strain can be measured directly from WGM measurements also outside this limit once the material parameters E and γ are known.

Therefore, to measure materials with a high Young's modulus (>10 kPa), small droplets (<20 µm) with high interfacial tension (>30 mN/m) should be used. Conversely, for soft materials large droplets and low interfacial tension are required. Using these parameters in an experimentally achievable range and taking into account the error of the deformation measurement via WGMs, the measurable Young's modulus range is 1-35 000 Pa (Supplementary Information). Importantly, note that this range spans across most soft human tissues, from mucus 10 Pa to a part of the muscle tissue 5-150 kPa, however, it is out of range for stiffer tissues such as epidermis, heart muscle and some tumors [54].

Biological tissues

After validation using hydrogels, the method was applied to biological tissues. Small pieces of mouse brain tissue ($\sim$1 mm^3) were embedded in the same gelatin hydrogel as used above. A glass microcapillary with a 0.5 µm inner diameter was used to inject oil droplets into the brain gray matter and the surrounding hydrogel (Figure 5a-c). The droplets were injected close to the interface between the brain and hydrogel (up to $\sim$ 50 µm) so that they could be easily imaged. The use of microcapillary makes the method minimally invasive and non-contact after the droplets have been injected. The droplets could also be premixed with the precursor cells when studying for example organoid growth in vitro. In this case, the method would be completely non-invasive. The hydrogel, which contained the brain tissue, was deformed by a movable container wall. The spectra from droplets in the brain tissue as well as in the hydrogel were measured before and after the external deformation was applied (Figure 5d). Initially, the droplets were already deformed. From the deformation, the initial internal stress (force) acting within the tissue was determined by using the Laplace equation [16]. The anisotropic stress in the plane perpendicular to the observation is measured to be $\Delta\sigma = 0.080 \pm 0.003$ nN/µm^2. The smallest anisotropic stress that can be measured is limited by the smallest measurable droplet deformation, the size of the droplet, and the interfacial tension. For a typical case, it is in the order of a few pN/µm^2.

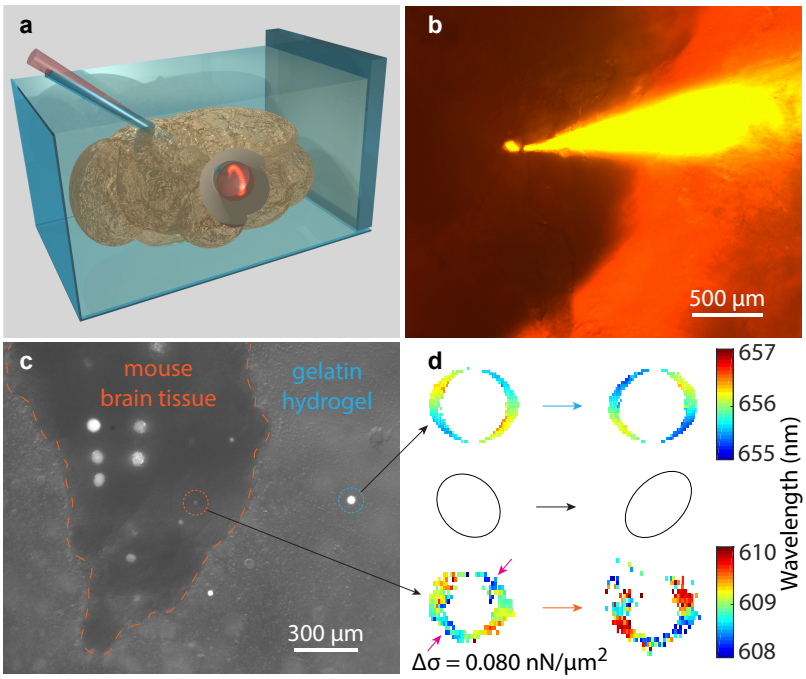

Figure 5. Measurement of stiffness and forces in brain tissue. **(a)** Schematic illustration of the experimental setup for measuring mechanics of mouse brain tissue, where an oil droplet is injected into the brain tissue contained within gelatin hydrogel. **(b)** Fluorescence image of a microcapillary at the moment of separation from the generated droplet in the brain tissue. **(c)** Multiple droplets at various positions in the brain tissue as well as in the surrounding gelatin hydrogel. **(d)** Wavelength shifts of a single WGM peak for the droplets in gelatin (top) and in brain tissue (bottom).

In order to measure Young's modulus of the brain tissue, an external deformation was applied to the brain tissue embedded inside the hydrogel. In general, the tissue can have a different stiffness than the hydrogel, therefore the strain in the tissue can be different than in the hydrogel. For that reason, the local strain was measured by the change in the relative positions of multiple droplets injected into the brain as well as other

visual reference points of the brain tissue. Interfacial tension of oil droplets in brain tissue was measured by the maximum bubble pressure tensiometry method. The maximum pressure was approximately two times smaller than in the hydrogel while using the same microcapillary, giving an interfacial tension of $35 \pm 3\,\mathrm{mN/m}$. A lower interfacial tension compared to just gelatine is expected due to the presence of various surfactants in tissues.

The WGM shifts caused by the applied external strain indicate that both the direction and the magnitude of the droplet deformation changed (Figure 5d). From this change, the measured strain and the interfacial tension, Young's modulus was measured to be $4.9 \pm 1\,\mathrm{kPa}$ for the droplet in Figure 5c. This is comparable to the values for mouse brain from the literature 1-10 kPa [43–45]. Because multiple droplets were embedded into the tissue and the surrounding hydrogel (Figure 5c), a distinct difference in Young's modulus at both positions was measured. With multiple droplets, Young's modulus could even be mapped in 3D, although limited by the concentration of the embedded droplets.

For practical applications, such as in vivo measurements, the maximum depth in the tissue where the method still works is very important. Because the spectral imaging is very similar to a regular confocal microscope, the penetration depth should also be very similar. To test the depth of penetration, imaging through optical phantoms with known scattering properties was performed. The properties of the phantoms were measured by an integrating sphere. At an optical thickness of 6 mean free paths the shape of the droplet could be easily determined by measuring the spectral shifts. The maximum depth was estimated to be approximately 10 mean free paths, which is also the commonly acknowledged depth limit of imaging techniques using ballistic photons [55]. The 6 and 10 mean free paths correspond to 400 µm and 670 µm in the mammalian cerebral cortex, respectively. By using a pulsed laser it was possible to measure the WGM spectra up to a depth of 20 mean free paths, corresponding to 1300 µm in the mammalian cerebral cortex. At this depth, it was not possible to capture a hyperspectral scan, but still mode splitting was observed (Supplementary Figure 4), which may also be used to estimate the droplet deformation.

We have also recently demonstrated that the microcavity spectrum can be detected from as deep as 3.5 transport lengths [56], which corresponds to 3.5 mm in the mammalian cerebral cortex at a wavelength of 620 nm. The potential use of two-photon excitation [57, 58] would improve the maximum depth even further.

Further directions

In this study, a single hyperspectral image of the droplet is used to determine the droplet shape and the anisotropic stress in the plane perpendicular to the observer direction. However, using hyperspectral images from multiple directions, the deformation along all three semi-axes of the ellipsoid and its orientation could be uniquely determined for an arbitrary deformation. This would be useful in more complex biological environments, where internal strains are less homogeneous.

In general, the new method is expected to work for all the cases where confocal microscopy is applicable. There is a broad selection of tools available for confocal microscopy in vivo, such as immobilization devices and cranial windows. The most limiting factor is the light penetration, which is the same limitation as for confocal microscopy. However it is still useful for smaller organisms and embryos; for example, imaging of droplet shapes was shown in live embryos [16].

Beyond the demonstrated applications, the developed method and WGM droplet microcavities could be simultaneously employed as mechanical sensors, refractive index sensors, and spectral barcodes. While our

method does not require prior knowledge of the refractive index for either the droplet or the external medium, if one refractive index is known, then both the diameter and the other refractive index can be determined by fitting the WGMs. [49]. Because the droplet refractive index is known, the external refractive index can be measured. In this way for example the water content of hydrogels and biological materials could be measured, which is in turn also important for their mechanical properties. Further, WGM microcavities have been shown to be a very powerful way of barcoding, especially for cell tagging and tracking [59–61]. For spherical cavities, the diameter is used as the unique identifier. For droplets that can deform, alternatively, the volume could be used as the unique identifier.

Conclusions

We have demonstrated that droplets supporting WGMs are an exceptionally precise and versatile method for studying biomechanical forces and stiffness at the microscale. Our method offers significant advantages for investigating the mechanical properties of biological tissues.

Firstly, our method allows for long-term measurements of mechanical properties in 3D biological tissues without requiring significant contact with an artificial material, as is the case with most other force measurement methods such as AFM and traction force microscopy. This makes it possible to obtain measurements of mechanical properties in biological tissues over extended periods of time. Secondly, our method by combining maximum bubble pressure tensiometry and droplet deformation measurements enables simultaneous measurement of Young's modulus, magnitude and direction of strain, interfacial tension of oil droplets embedded in tissue, as well as the intrinsic internal anisotropic stress (force) within the tissues. To the best of our knowledge, no other technique can measure all of these quantities simultaneously. Thirdly, absolute values of all of the quantities mentioned above can be measured without making assumptions about the tissue. Our method requires only the inner diameter of the microcapillary used for the injection to be known in advance and no additional measurements outside this setup are needed. Fourthly, by injecting multiple droplets our method allows for the mechanical properties of tissues to be measured at different positions across the tissues. The droplets used here are of cell size ($\sim 10\,\mu m$), therefore enabling very localized measurements and in the future will allow for 3D mapping of mechanical properties and measurement within single cells [41]. Fifthly, the new method enables the measurement of Young's modulus in a very wide range of values from 1 Pa to 35 kPa. Notably, the determination of Young's modulus of very soft materials (<1 kPa) is difficult [46].

Overall, our droplet microcavity method provides an innovative approach for measuring the stiffness and forces in biological tissues with high accuracy and versatility. The ability to jointly measure a quite unique set of mechanical parameters can significantly complement other established methods and has high potential in the field of biomechanics by enabling the study of a wide range of mechanical aspects of biological tissues, both in vitro and in vivo.

Materials and Methods

Sample preparation

Gelatin from porcine skin (gel strength 90-110 g, Sigma Aldrich, Germany) was dissolved in PBS (phosphate buffered saline) at a concentration of 8.5 %w/w. The solution was briefly elevated to 90°C and then filtered

by 0.2 µm syringe filter. Polyphenyl ether oil (Santolubes, USA, SL5262, $n = 1.62$) doped with 0.1 %w/w fluorescent dye (pyrromethene 597, Exciton, USA) was mechanically stirred into the liquid gelatin to form polydispersed droplets. SL5262 oil is also compatible with standard lipophilic biocompatible dyes [62], which would be more suitable for live samples. To get the brain tissue, the mouse head was decapitated, and the skin from the upper part of the head was removed, followed by the removal of the skull and brain with a scalpel and tweezers. Only tissues of mice euthanized for other ethically approved studies were used.

A rectangular container with dimensions 21.6 mm × 23.8 mm (2-well μ-chamber, Ibidi, Germany) was used. A glass slide fixed to a motorized linear stage (MFA-CC, Newport) was inserted vertically into the container. First a 1.5 mm thick hydrogel layer without dispersed microdroplets was poured into the container and left to solidify. A gelatin solution with dispersed microdroplets at 27°C was added, to a combined total height of 3 mm. The sample was shut air-tight with para-film foil, and in the neighboring chamber, a sponge soaked with water was put to prevent the hydrogel from drying. After the gelation of the hydrogel, the sample was left to rest for another ~ 4 hours before measurements. Samples containing mouse brain tissue were prepared using the same method and experimental setup. Instead of hydrogel containing oil droplets, it contained pieces of mouse brain tissue. Oil droplets were injected afterward using a 0.5 µm inner diameter microcapillaries. The microcapillary moved through soft gelatin with ease, and droplet creation inside the gelatin and brain tissue was performed by applying pressure to the oil inside the microcapillary. Typically, the minimum pressure needed to inject droplets into gelatin and the brain was 1300 mbar and 750 mbar, respectively.

Optical setup

Microdroplets were illuminated by green LED (CoolLED, UK, pE-300, 0.5-20 mW) through a 20 × objective (0.45 NA). The fluorescent light was collected through the same objective and sent simultaneously to an imaging spectrometer (Andor, UK, Shamrock 500i) with 10 µm input slit width and a grating of 1200 lines per millimeter. The effective collection NA was 0.23 due to using the microscope's internal magnification. Fluorescence image of a wider field of view was imaged beforehand with a digital camera (Andor, UK, sCMOS Zyla 4.2) with a 4 × objective. To capture a hyperspectral image, each droplet was scanned with the push-broom technique. This involves capturing spatially resolved spectra along the spectrometer slit and moving the sample in steps to capture spectra for each point of the image. The spatial pixel resolution of the hyperspectral image was $\sim 0.5 \times 0.5\,\mu m^2$. For faster scanning, the scan was made with steps of 1 µm. The motorized microscope stage was used to automatically travel between positions of individual droplets to perform the hyperspectral imaging on each of them.

Young's modulus

As an independent measurement, Young's modulus of the hydrogel was measured with the indentation method using the Hertz model [63]. A 1 mm diameter glass capillary with spherical tip shape was used to probe 20 mm × 20 mm × 10 mm hydrogel sample at room temperature. Indentation depth was imaged with a camera and force measurement was performed by Metler Toledo balance with 0.01 mN accuracy.

Simulations

Simulations were implemented with a finite elements method using an open source python library FEniCS [64]. An open-source 3D finite element mesh generator Gmsh [65] was used to generate a non-uniform 3D mesh (Supplementary Figure 5). Typically, the size of the simulation box was 10× larger than the diameter of the droplet so that the effects of a finite simulation box are negligible. To reproduce the experiment, a cube of elastic material (hydrogel) was simulated with an initially spherical liquid inclusion, which represents a section of the hydrogel around a single inclusion (Figure 2a). The external hydrogel strain is implemented by the Dirichlet boundary condition for the strain at the boundary surfaces. The relaxed structure is numerically calculated by minimization of total free energy using Newton's iterative method. The total free energy consists of the linear elastic free energy of the hydrogel and the interfacial tension free energy term, while the incompressibility of the liquid inclusion was taken into account by a constraint on the deformation at the droplet surface using the method of Lagrange multipliers. The detailed mathematical formulation of the problem is in the Supplementary Information.

Acknowledgments

This project has received funding from the European Research Council (ERC) under the European Union's Horizon 2020 research and innovation programme (grant agreement No. 851143), from Human Frontier Science Program (RGY0068/2020), and from Slovenian Research Agency (ARRS) (J1-1697, N1-0195, J1-2462, PR-08969 and P1-0099).

Data Availability Statement

The data that support the findings of this study are available from the corresponding author upon reasonable request.

Author contributions

M.H. and M.R. designed research; G.P. and M.M. performed research; G.P. and M.M. analyzed data; G.P., M.M., M.R. and M.H. wrote the paper.

References

[1] Pierre-Gilles De Gennes and Jacques Prost. *The physics of liquid crystals*. Number 83. Oxford university press, 1993.

[2] Yasuyuki Kimura. Microrheology of soft matter. *J. Phys. Soc. Jpn.*, 78(4):041005–041005, 2009.

[3] Ilya Levental, Penelope C Georges, and Paul A Janmey. Soft biological materials and their impact on cell function. *Soft Matter*, 3(3):299–306, 2007.

[4] Hoi Ki Cheung, Tim Tian Y Han, Dale M Marecak, John F Watkins, Brian G Amsden, and Lauren E Flynn. Composite hydrogel scaffolds incorporating decellularized adipose tissue for soft tissue engineering with adipose-derived stem cells. *Biomaterials*, 35(6):1914–1923, 2014.

[5] FuiBoon Kai, Hanane Laklai, and Valerie M Weaver. Force matters: biomechanical regulation of cell invasion and migration in disease. *Trends Cell Biol.*, 26(7):486–497, 2016.

[6] Xin Chen, Moxiao Li, Mao Yang, Shaobao Liu, Guy M Genin, Feng Xu, and Tian Jian Lu. The elastic fields of a compressible liquid inclusion. *Extreme Mech. Lett.*, 22:122–130, 2018.

[7] Pere Roca-Cusachs, Vito Conte, and Xavier Trepat. Quantifying forces in cell biology. *Nat. Cell Biol.*, 19(7):742–751, 2017.

[8] Thomas Lanzicher, Valentina Martinelli, Carlin S. Long, Giorgia Del Favero, Luca Puzzi, Massimo Borelli, Luisa Mestroni, Matthew R.G. Taylor, and Orfeo Sbaizero. AFM single-cell force spectroscopy links altered nuclear and cytoskeletal mechanics to defective cell adhesion in cardiac myocytes with a nuclear lamin mutation. *Nucleus*, 6(5):394–407, 2015.

[9] Juliet Lee, Michelle Leonard, Tim Oliver, Akira Ishihara, and Ken Jacobson. Traction forces generated by locomoting keratocytes. *J. Cell Biol.*, 127(6 II):1957–1964, 1994.

[10] V. Maruthamuthu, B. Sabass, U. S. Schwarz, and M. L. Gardel. Cell-ECM traction force modulates endogenous tension at cell-cell contacts. *Proc. Natl. Acad. Sci. U.S.A.*, 108(12):4708–4713, 2011.

[11] Robert W Style, Rostislav Boltyanskiy, Guy K German, Callen Hyland, Christopher W MacMinn, Aaron F Mertz, Larry A Wilen, Ye Xu, and Eric R Dufresne. Traction force microscopy in physics and biology. *Soft matter*, 10(23):4047–4055, 2014.

[12] O. du Roure, A. Saez, A. Buguin, R. H. Austin, P. Chavrier, P. Silberzan, and B. Ladoux. Force mapping in epithelial cell migration. *Proc. Natl. Acad. Sci. U.S.A.*, 102(7):2390–2395, 2005.

[13] Marita L. Rodriguez, Patrick J. McGarry, and Nathan J. Sniadecki. Review on Cell Mechanics: Experimental and Modeling Approaches. *Appl. Mech. Rev.*, 65(6):060801, 2013.

[14] Hu Zhang and Kuo-Kang Liu. Optical tweezers for single cells. *J. R. Soc., Interface*, 5(24):671–690, 2008.

[15] Robert Prevedel, Alba Diz-Muñoz, Giancarlo Ruocco, and Giuseppe Antonacci. Brillouin microscopy: an emerging tool for mechanobiology. *Nat. Methods*, 16(10):969–977, 2019.

[16] Otger Campàs, Tadanori Mammoto, Sean Hasso, Ralph A Sperling, Daniel O'connell, Ashley G Bischof, Richard Maas, David A Weitz, Lakshminarayanan Mahadevan, and Donald E Ingber. Quantifying cell-generated mechanical forces within living embryonic tissues. *Nat. Methods*, 11(2):183–189, 2014.

[17] Friedhelm Serwane, Alessandro Mongera, Payam Rowghanian, David A Kealhofer, Adam A Lucio, Zachary M Hockenbery, and Otger Campas. In vivo quantification of spatially varying mechanical properties in developing tissues. *Nat. Methods*, 14(2):181–186, 2017.

[18] D Molino, S Quignard, C Gruget, F Pincet, Y Chen, M Piel, and J Fattaccioli. On-chip quantitative measurement of mechanical stresses during cell migration with emulsion droplets. *Sci. Rep.*, 6(1):1–11, 2016.

[19] Wontae Lee, Nikita Kalashnikov, Stephanie Mok, Ruba Halaoui, Elena Kuzmin, Andrew J Putnam, Shuichi Takayama, Morag Park, Luke McCaffrey, Ruogang Zhao, et al. Dispersible hydrogel force sensors reveal patterns of solid mechanical stress in multicellular spheroid cultures. *Nat. Commun.*, 10(1):1–14, 2019.

[20] Dadhichi Paretkar, Xuejuan Xu, Chung-Yuen Hui, and Anand Jagota. Flattening of a patterned compliant solid by surface stress. *Soft matter*, 10(23):4084–4090, 2014.

[21] Robert W Style, Anand Jagota, Chung-Yuen Hui, and Eric R Dufresne. Elastocapillarity: Surface tension and the mechanics of soft solids. *Annu. Rev. Condens. Matter Phys.*, 8:99–118, 2017.

[22] Robert W Style, Ravi Tutika, Jin Young Kim, and Michael D Bartlett. Solid–liquid composites for soft multifunctional materials. *Adv. Funct. Mater.*, 31(1):2005804, 2021.

[23] Paul Grandgeorge, Natacha Krins, Aurélie Hourlier-Fargette, Christel Laberty-Robert, Sébastien Neukirch, and Arnaud Antkowiak. Capillarity-induced folds fuel extreme shape changes in thin wicked membranes. *Science*, 360(6386):296–299, 2018.

[24] Xiying Li, Jia Ming Zhang, Xin Yi, Zhongyi Huang, Pengyu Lv, and Huiling Duan. Multimaterial microfluidic 3d printing of textured composites with liquid inclusions. *Adv. Sci.*, 6(3):1800730, 2019.

[25] Robert W Style, Ravi Tutika, Jin Young Kim, and Michael D Bartlett. Solid–liquid composites for soft multifunctional materials. *Adv. Funct. Mater.*, 31(1):2005804, 2021.

[26] Maria Vomero, Maria Francisca Porto Cruz, Elena Zucchini, Francesca Ciarpella, Emanuela Delfino, Stefano Carli, Christian Boehler, Maria Asplund, Davide Ricci, Luciano Fadiga, et al. Conformable polyimide-based μecogs: Bringing the electrodes closer to the signal source. *Biomaterials*, 255:120178, 2020.

[27] Jhulan Powrel and Narayan Prasad Adhikari. Elastic property of sickle and normal hemoglobin protein: Molecular dynamics. *AIP Adv.*, 12(4):045308, 2022.

[28] Matthew R Foreman, Jon D Swaim, and Frank Vollmer. Whispering gallery mode sensors. *Adv. Opt. Photonics*, 7(2):168–240, 2015.

[29] D. McGloin. Droplet lasers: A review of current progress. *Rep. Prog. Phys.*, 80(5), 2017.

[30] Van Duong Ta, Yue Wang, and Handong Sun. Microlasers Enabled by Soft-Matter Technology. *Adv. Opt. Mater.*, 7(17):1–30, 2019.

[31] Yan Wang, Hanyang Li, Liyuan Zhao, Bing Wu, Shuangqiang Liu, Yongjun Liu, and Jun Yang. A review of droplet resonators: Operation method and application. *Opt. Laser Technol.*, 86:61–68, 2016.

[32] Mitsunori Saito, Hiroya Shimatani, and Hideyuki Naruhashi. Tunable whispering gallery mode emission from a microdroplet in elastomer. *Opt. Express*, 16(16):11915, 2008.

[33] S. C. Yorulmaz, M. Mestre, M. Muradoglu, B. E. Alaca, and A. Kiraz. Controlled observation of nondegenerate cavity modes in a microdroplet on a superhydrophobic surface. *Opt. Commun.*, 282(14):3024–3027, 2009.

[34] Mehdi Aas, Alexandr Jonáš, Alper Kiraz, Oto Brzobohatỳ, Jan Ježek, Zdeněk Pilát, and Pavel Zemánek. Spectral tuning of lasing emission from optofluidic droplet microlasers using optical stretching. *Opt. Express*, 21(18):21380–21394, 2013.

[35] Rachel Symes, Robert M Sayer, and Jonathan P Reid. Cavity enhanced droplet spectroscopy: Principles, perspectives and prospects. *Phys. Chem. Chem. Phys.*, 6(3):474–487, 2004.

[36] Van Duong Ta, Rui Chen, and Han Dong Sun. Tuning whispering gallery mode lasing from self-assembled polymer droplets. *Sci. Rep.*, 3(1):1362, 2013.

[37] Tindaro Ioppolo, Michael Kozhevnikov, Vadim Stepaniuk, M Volkan Ötügen, and Valery Sheverev. Micro-optical force sensor concept based on whispering gallery mode resonators. *Appl. Opt.*, 47(16):3009–3014, 2008.

[38] Aidan Rafferty, Kyle Gorkowski, Andreas Zuend, and Thomas C. Preston. Optical deformation of single aerosol particles. *Proc. Natl. Acad. Sci. U. S. A.*, 116(40):19880–19886, 2019.

[39] Saverio Avino, Anika Krause, Rosa Zullo, Antonio Giorgini, Pietro Malara, Paolo De Natale, Hans Peter Loock, and Gianluca Gagliardi. Direct sensing in liquids using whispering-gallery-mode droplet resonators. *Adv. Opt. Mater.*, 2(12):1155–1159, 2014.

[40] Matthew R Foreman, Saverio Avino, Rosa Zullo, H-P Loock, F Vollmer, and G Gagliardi. Enhanced nanoparticle detection with liquid droplet resonators. *Eur. Phys. J.: Spec. Top.*, 223(10):1971–1988, 2014.

[41] Matjaž Humar and Seok Hyun Yun. Intracellular microlasers. *Nat. Photonics*, 9(9):572–576, 2015.

[42] Maurizio Manzo, Omar Cavazos, Erick Ramirez-Cedillo, and Hector R Siller. Embedded spherical microlasers for in vivo diagnostic biomechanical performances. *ASME J. Eng. Sci. Med. Diagn. Ther.*, 3(4):044504, 2020.

[43] Yuan Feng, Yuan Gao, Tao Wang, Luyang Tao, Suhao Qiu, and Xuefeng Zhao. A longitudinal study of the mechanical properties of injured brain tissue in a mouse model. *J. Mech. Behav. Biomed. Mater.*, 71:407–415, 2017.

[44] T Kaster, Ira Sack, and Afshan Samani. Measurement of the hyperelastic properties of ex vivo brain tissue slices. *J. Biomech.*, 44(6):1158–1163, 2011.

[45] G Soza, R Grosso, Ch Nimsky, P Hastreiter, R Fahlbusch, and G Greiner. Determination of the elasticity parameters of brain tissue with combined simulation and registration. *Int. J. Med. Robot. Comput. Assist. Surg.*, 1(3):87–95, 2005.

[46] Kerstyn Comley and Norman A Fleck. A micromechanical model for the young's modulus of adipose tissue. *Int. J. Solids Struct.*, 47(21):2982–2990, 2010.

[47] Robert W Style, Rostislav Boltyanskiy, Benjamin Allen, Katharine E Jensen, Henry P Foote, John S Wettlaufer, and Eric R Dufresne. Stiffening solids with liquid inclusions. *Nat. Phys.*, 11(1):82–87, 2015.

[48] C Franck, S Hong, SA Maskarinec, DA Tirrell, and G Ravichandran. Three-dimensional full-field measurements of large deformations in soft materials using confocal microscopy and digital volume correlation. *Exp. Mech.*, 47(3):427–438, 2007.

[49] Jay D Eversole, H-B Lin, AL Huston, Anthony J Campillo, Peter T Leung, SY Liu, and Kenneth Young. High-precision identification of morphology-dependent resonances in optical processes in microdroplets. *J. Opt. Soc. Am. B*, 10(10):1955–1968, 1993.

[50] Aliyar Javadi, N Mucic, Mohsen Karbaschi, Jooyoung Won, VB Fainerman, A Sharipova, EV Aksenenko, VI Kovalchuk, NM Kovalchuk, Jürgen Krägel, et al. Inferfacial dynamics methods. In *Encyclopedia of Colloid and Interface Science*, pages 637–676. Springer, 2013.

[51] CA MacLeod and CJ Radke. A growing drop technique for measuring dynamic interfacial tension. *J. Colloid Interface Sci.*, 160(2):435–448, 1993.

[52] Brendan F Kennedy, Philip Wijesinghe, and David D Sampson. The emergence of optical elastography in biomedicine. *Nat. Photonics*, 11(4):215–221, 2017.

[53] John Douglas Eshelby. The determination of the elastic field of an ellipsoidal inclusion, and related problems. *Proc. R. Soc. London, Ser. A*, 241(1226):376–396, 1957.

[54] Carlos F Guimarães, Luca Gasperini, Alexandra P Marques, and Rui L Reis. The stiffness of living tissues and its implications for tissue engineering. *Nat. Rev. Mater.*, 5(5):351–370, 2020.

[55] Najva Akbari, Mihailo R Rebec, Fei Xia, and Chris Xu. Imaging deeper than the transport mean free path with multiphoton microscopy. *Biomed. Opt. Express*, 13(1):452–463, 2022.

[56] Aljaž Kavčič, Maja Garvas, Matevž Marinčič, Katrin Unger, Anna Maria Coclite, Boris Majaron, and Matjaž Humar. Deep tissue localization and sensing using optical microcavity probes. *Nat. Commun.*, 13(1):1269, 2022.

[57] Evgeniy A Mamonov, Anton I Maydykovskiy, Nikolai V Mitetelo, Dasari Venkatakrishnarao, Rajadurai Chandrasekar, and Tatyana V Murzina. Whispering gallery modes in two-photon fluorescence from spherical dcm dye microresonators. *Laser Phys. Lett.*, 15(3):035401, 2018.

[58] Nikolai V Mitetelo, Mikhail E Popov, Evgeniy A Mamonov, Anton I Maydykovskiy, Dasari Venkatakrishnarao, Jada Ravi, Rajadurai Chandrasekar, and Tatiana V Murzina. Chirality driven effects in multiphoton excited whispering gallery mode microresonators prepared by a self-assembly technique. *Laser Phys. Lett.*, 17(3):036201, 2020.

[59] Matjaž Humar, Avinash Upadhya, and Seok Hyun Yun. Spectral reading of optical resonance-encoded cells in microfluidics. *Lab Chip*, 17(16):2777–2784, 2017.

[60] Allon M Klein, Linas Mazutis, Ilke Akartuna, Naren Tallapragada, Adrian Veres, Victor Li, Leonid Peshkin, David A Weitz, and Marc W Kirschner. Droplet barcoding for single-cell transcriptomics applied to embryonic stem cells. *Cell*, 161(5):1187–1201, 2015.

[61] Nikita Toropov and Frank Vollmer. Whispering-gallery microlasers for cell tagging and barcoding: the prospects for in vivo biosensing. *Light: Sci. Appl.*, 10, 2021.

[62] Tkhe Kyong Fam, Andrey S Klymchenko, and Mayeul Collot. Recent advances in fluorescent probes for lipid droplets. *Materials*, 11(9):1768, 2018.

[63] Stylianos-Vasileios Kontomaris. The hertz model in afm nanoindentation experiments: applications in biological samples and biomaterials. *Micro Nanosyst.*, 10(1):11–22, 2018.

[64] G. N. Wells et al A. Logg, K.-A. Mardal. *Automated Solution of Differential Equations by the Finite Element Method*. Springer, 2012.

[65] Geuzaine, Christophe and Remacle, Jean-Francois. Gmsh.